

Ground Base Station Antenna Design for Air-to-Ground Communications

Lucas Nogueira Ribeiro, Sertan Hastürkoğlu, Jan Grävendieck
Ericsson Antenna System, Rosenheim, Germany

{lucas.nogueira.ribeiro, sertan.hasturkoglu, jan.graevendieck}@ericsson.com

Abstract—The sixth generation (6G) of mobile communication networks aims to bring innovations in mobile broadband solutions and airborne communications. This paper proposes an antenna solution for direct air-to-ground (ATG) communications, particularly focusing on the challenges and potential of the digital airspace vision. The intra- and inter-cell interference caused by sidelobes of ground base station (BS) antennas and the bandwidth constraints at sub-6 GHz bands are important limitations. The paper introduces a ground BS antenna design for the 5.9-8.5 GHz band. The main contributions include wide-band, high-isolation antenna array concept for the ground BS antenna, along with an analysis of how the antenna array dimension affects the signal-to-noise-and-interference ratio and throughput in ATG systems.

Index Terms—6G, ATG, antennas, cmWave, coverage analysis

I. INTRODUCTION

The sixth generation (6G) of mobile communication networks is expected to extend the 5G ecosystem to foster innovations that bring value to mobile network operators and simplify network operation [1], [2]. Ericsson’s 6G research vision [3] describes the technological foundations for the future mobile communication networks of the 2030s. New spectrum, non-terrestrial access, and multi-connectivity are identified as key enablers of improved network performance and coverage. The development of the digital airspace [4] is therefore important to enable non-terrestrial access in a reliable manner. For instance, a holistic approach to integrate terrestrial and non-terrestrial networks has been under development in the 6G SKY project [5].

The digital airspace offers new opportunities in the sky, such as mission-critical mobile broadband solutions and high altitude communication for aircraft [4]. In the latter use case, ground base station (BS) antennas provide high capacity links to aircraft flying from 3 km to 10 km of altitude. In fact, this technology has been known for years as direct air-to-ground (ATG) communications [6] and there exist solutions provided by Gogo Networks [7], Alcatel Lucent (Nokia) [8], and European Aviation Network (EAN) [9]. Furthermore, there have been various studies on the design and optimization of ATG networks. The impact of different passive antenna arrays on LTE-based ATG systems has been investigated in [10]. The paper provides insights into the cell volume shape, signal-to-noise-and-interference ratio (SINR) histograms for different altitude, and the corresponding throughput. Since then, massive MIMO and 5G NR-based solutions have been investigated in the ATG context [11], [12].

The evolution of ATG networks targeting improved data throughput and reliability requires solutions for various technical challenges. For example, sidelobes of the ground BS

antenna cause intra- and inter-cell interference and raise concerns about the coexistence with fixed satellite services and terrestrial networks [13], [14]. Moreover, the operation at sub-6 GHz bands imposes a limitation on the maximum system bandwidth, which then upper limits the achievable throughput. The cmWave frequency range, defined from 7 GHz to 15 GHz, potentially strikes a balance capacity and propagation losses, being a promising frequency range for 6G [2].

The ground BS antenna design is clearly central to addressing these technical challenges. To this end, this paper proposes a novel ground BS antenna design for the cmWave range. More specifically, the main contributions of this paper are: (i) a novel wide-band and high-isolation antenna array concept for the cmWave range band, and (ii) new insights on how ground BS antenna array dimension influences the SINR and throughput performance of ATG systems.

The paper is organized as follows. The novel ground BS antenna design and its far-field pattern as well as S-parameter performance are presented in Section II. The system-level evaluation of the proposed antenna design and insights into the coverage optimization of ATG systems are discussed in Section III.

II. GROUND BASE STATION ANTENNA ARRAY

In antenna array design, the elimination of unwanted resonances within the desired frequency band is critical. Particularly in densely packed active antenna systems, coupling between radiating elements can induce resonances that adversely affect scattering parameters and far-field patterns. Broadly three major resonances can occur: standard grating lobe resonances, Floquet wave poles, and common mode resonances [15].

Given these challenges, the patch antenna design emerged as the preferred choice for BS antennas. Its inherent ability to shift resonances outside the active frequency band gives it an advantage. In contrast to dipole radiators, the novel patch radiator exhibits superior directivity and is vertically compact, resulting in a slim array profile. Electromagnetic simulations confirm that slots on the radiator surface reposition resonances within the targeted frequency band of 5.9-8.5 GHz, making it an ideal BS antenna in this range. A stand-alone representation is shown in Figure 1.

As an example, assume the ground BS antenna array design in Figure 2, comprising $M_H = 4$ columns each with $M_V = 9$ rows of $\pm 45^\circ$ -polarized radiators. Considering the array of sub-array (AoSA) model [16], the radiators are grouped into sub-arrays of N_V rows and N_H columns. Each antenna sub-array is then fed by one RF branch per polarization. Therefore, such array of sub-arrays is fed by $\lfloor M_V/N_V \rfloor \times \lfloor M_H/N_H \rfloor$ RF

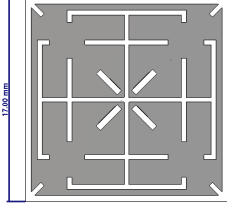


Fig. 1. Standalone radiator with a head size of 17 mm and height of 6.52 mm.

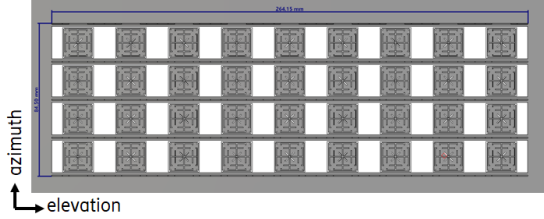


Fig. 2. Antenna array designed for the 7 GHz carrier frequency with 4 columns and 9 radiators per column. The second and third columns are referred to as center columns.

branches per polarization. The column spacing is 0.51λ and a vertical spacing of 0.72λ , where λ denotes the free space wavelength at 7 GHz. This design facilitates directional beam-forming, allowing individual column operations for multiple targets. Figure 2 provides an overall view of the 84.5×264.15 mm² array antenna, comprising 36 dual-polarized radiators in total.

Array decoupling surface (ADS) is a technology that enhances the isolation between radiating elements in an antenna array [17]. The proposed ground BS antenna design uses an ADS to increase radiator isolation and minimize mutual coupling. Figure 3 shows an aerial view of the antenna array together with the ADS. Essentially, the ADS uses an array of non-resonant passive elements above the radiators. These small reflective surfaces, mounted on a circuit board, are designed to achieve higher decoupling by superposition of the direct path between the radiators and the second reflective path from the ADS.

The performance evaluation of the ground BS antenna considers two figures of merit: scattering (S) parameters and far-field directivity. Each column of the (9×4) array is grouped into 3 sub-arrays of (3×1) radiators. The sub-arrays in each column are jointly fed to form a single beam per polarization. In the simulation results, Ports 1 and 2 refer to $+45^\circ$ and -45° polarization ports of one of the central columns, respectively, and Port 3 refers to the $+45^\circ$ polarization port of the adjacent central column. Therefore, S_{11} and S_{22} denote the active input reflection coefficients of both linear polarizations and S_{21} the coupling between the cross-polarized ports in the same column. Furthermore, S_{13} and S_{23} represent the coupling for co- and cross-polarized ports between the adjacent central columns, respectively.

The simulated S parameters magnitude are shown in Figure 4. The active input reflection coefficients show a value below -15 dB for the frequency range of, where this value

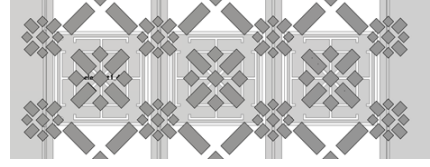


Fig. 3. Array decoupling surface above the patch radiators.

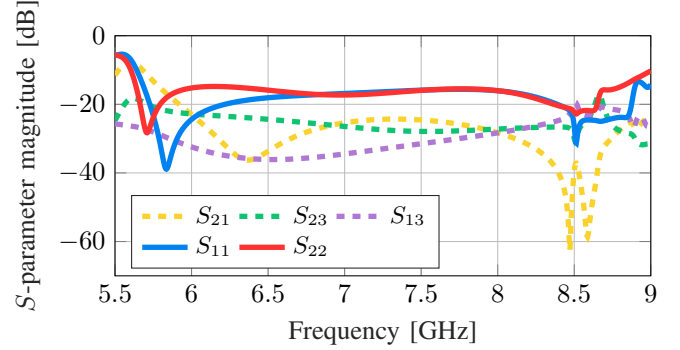


Fig. 4. S_{11} and S_{22} denote the input reflection coefficients for different polarizations in the same antenna array column. S_{21} is the decoupling between cross-polarized ports in the same column, while S_{13} and S_{23} refer to the decoupling in different adjacent columns with co- and cross-polarized ports, respectively.

refers to a boresight. Achieved decoupling is about -20 dB at the beginning of the frequency band and values below -20 dB are attained at the higher frequencies within the band of interest. The far-field characteristics of a single antenna port are evaluated for two vertical beam tilting angles: 2° and 12° in Figures 5 and 6, respectively. It can be seen from these vertical cut plots that the directivity varies from 13.8 dBi to 16.4 dBi. Also, grating lobes become more visible in the scenario with 12° uptilt, nevertheless these undesired lobes can be attenuated by feeding amplitude tapering or alternative methods, such as irregular sub-array geometries [18]. The study of sidelobe attenuation for ATG application is out of the scope of this contribution and shall be considered in future work.

III. SYSTEM-LEVEL EVALUATION

System-level simulations were performed to study the influence of the ground BS antenna array parameters on the overall system-level performance indicators. The downlink SINR and both the downlink and uplink data throughput are considered as figures of merit in the performed simulations. The empirical cumulative distribution function (cdf) of these figures of merit are calculated for each simulation and compared for different combination of independent antenna parameters. Furthermore, plots of the combined antenna and propagation gains were also calculated to provide visualization of the cell coverage. The independent variables of the simulation campaign are

- 1) The vertical antenna element spacing d_V . It was set to either 0.5λ or 0.7λ , where λ denotes the carrier wavelength.
- 2) The sub-array dimensions $N_V \times N_H$ of the antenna array. Either (9×1) or (3×1) sub-arrays set used in

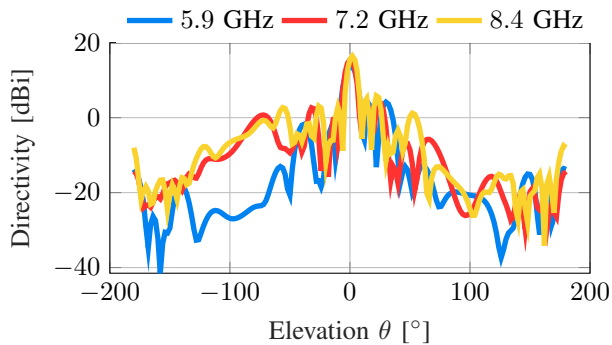


Fig. 5. Far-field directivity of single antenna array port exciting 9 radiators and 2° up tilt for different frequencies.

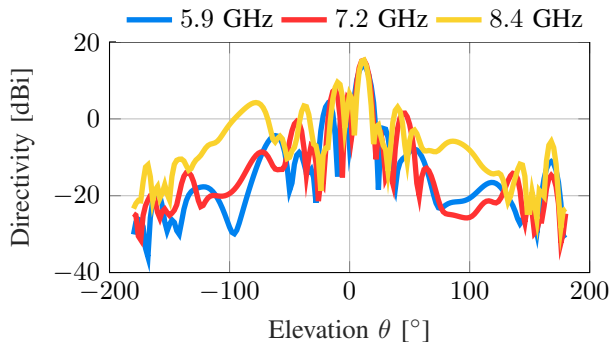


Fig. 6. Far-field directivity of single antenna array port exciting 9 radiators and 12° up tilt for different frequencies.

the simulations. The former array configuration forms narrower than the latter, and operates at lower MIMO orders than the latter for a fixed number of antenna radiators [16].

Two ground BS deployment scenarios were considered in the simulation campaign. The parameters considered in both scenarios are shown in Table I. In the first deployment scenario, the BSs are deployed in a linear arrangement along the x axis with a fixed inter-site distance of 50 km and the flying terminals were uniformly distributed within the positive xz half-plane up to 15 km of altitude. A sweep over the simulation independent parameters provides insight into the influence of the ground BS antenna design on the figures of merit. In the second deployment scenario, the European Aerial Network (EAN) in Germany is modeled. The position of each ground BS site was derived from the information available at [9]. Each site was then modeled considered to have 3 sectors with the same transmit power. With such a deployment, it is possible to assess how the investigated antenna designs would perform in a real-life aerial network deployment.

A. Uniform Linear Deployment

In this scenario, the four possible combinations of the independent variables are tested considering high cell load, mechanical up tilt, and a single beam obtained from uniform array phasing. The obtained antenna and propagation gain plots are shown in Figure 7 and the empirical cdf plots are shown in Figures 8 and 9.

TABLE I
SYSTEM-LEVEL SIMULATION PARAMETERS

Parameter	Value
Ground BS height	30 meters
Ground BS maximum transmit power	53 dBm
Ground BS noise figure	5 dB
Ground BS beamforming scheme	Eigen-beamforming
Ground BS antenna configuration	9×4 dual-polarized radiators
Ground BS EIRP	74.5 dBm
ATG user speed	1200 km/h
ATG user maximum transmit power	40 dBm
ATG user noise figure	9 dB
ATG user antenna	Isotropic radiator
Number of ground BS sites	Scenario dependent
Number of sectors per site	3
Inter-site distance (ISD)	Scenario dependent
Wrap-around deployment	No
Mechanical up tilt	15°
Carrier frequency	7 GHz
Carrier bandwidth	100 MHz
Subcarrier spacing	30 kHz
Duplex scheme	TDD
TDD ratio	60% downlink, 40% uplink
Traffic model	Full buffer
Cell load	Low (10%) or high (100%)
Highest modulation scheme	256 QAM
MIMO mode	Single-user MIMO
Propagation model	Free-space path loss

A visual inspection of the gain plots in Figure 7 reveals the overlapping cell configuration discussed in [13], [14]. The immediate aerial region above one site is covered by its adjacent site. This helps the individual ground BSs keeping the beam steering range limited. Furthermore, these plots reveal an important influence of the sub-array size on cell coverage. For example, the (9×1) sub-array setup provides sharp beams that cause coverage “holes.” By contrast, (3×1) sub-arrays provide larger beams and offer a more spatially homogeneous coverage. Furthermore, the sidelobes of the (9×1) sub-array cause a less homogeneous coverage, which can lead to handover issues [19]. These visual insights are confirmed by the downlink SINR empirical cdf plots in Figures 8 and 9. The antenna configurations with larger sub-array outperformed the smaller ones. These simulation results also indicate that the vertical element spacing had minor influence on the downlink SINR performance, although larger separation yield sharper beams.

B. EAN Deployment in Germany

According to simulation results discussed in Section III-A, the vertical inter-element spacing does not significantly influence the system performance. Therefore, the investigations performed in the EAN deployment scenario considered only 0.7λ vertical element separation. The combined antenna and path gain patterns for different altitude levels and sub-array configurations are plotted in Figures 10 and 11. The effects of the antenna beamwidth on the combined gain pattern coverage are clear in these figures. Narrower beams, as those produced by the (9×1) configuration, leave uncovered “holes” in the space, while wider beams, such as those of the (3×1) configuration, better distributes the radiation energy in the space.

These results also provide some insight into the cell volume shape. Although the coverage area at different altitude levels

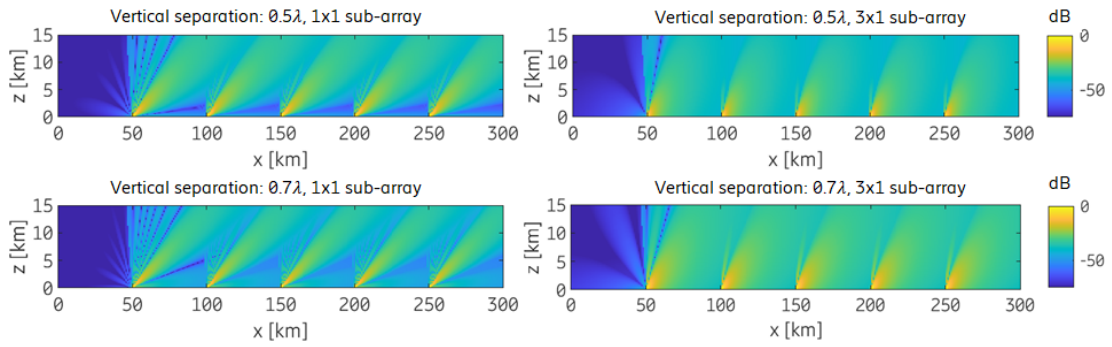


Fig. 7. Normalized combined antenna and path gain coverage plots for a fixed equal-phase beam and 15° of mechanical uptilt.

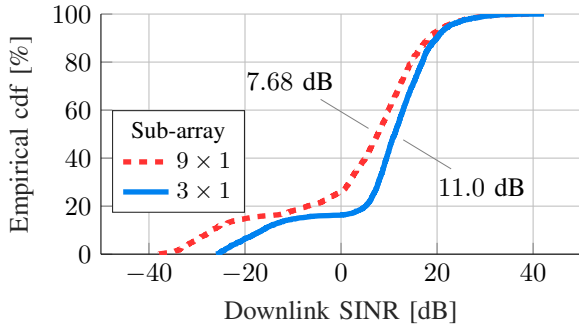


Fig. 8. Empirical cdf distribution of downlink SINR for antenna array vertical separation distance of 0.5λ . The median SINR values are indicated in the plot.

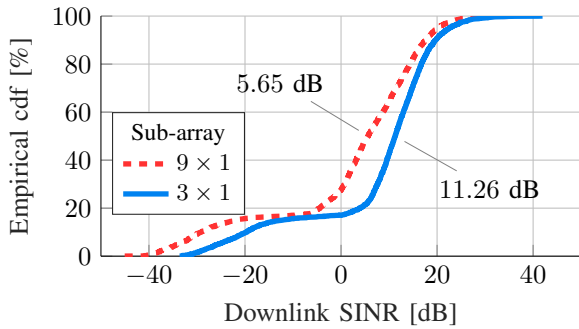


Fig. 9. Empirical cdf distribution of downlink SINR for antenna array vertical separation distance of 0.7λ . The median SINR values are indicated in the plot.

differs for both sub-array configurations, the cell areas of the (3×1) configuration seems to be more regular than those of the (9×1) . This indicates that the cell volume in the former configuration can be approximated by a prism, similar to what was reported in [10]. It remains to be verified in what other conditions this observation still holds.

Figures 10 and 11 also show that lower altitudes exhibit poor coverage compared to higher altitudes in the considered simulation setup. Therefore, it is reasonable to focus on a single altitude level at 10 km to assess the system throughput performance. Considering a uniform flying terminal deployment at this altitude, the obtained empirical cdf plots for the downlink and uplink throughput under different cell loads are shown in Figures 12 and 13, respectively. The impact of the sub-array

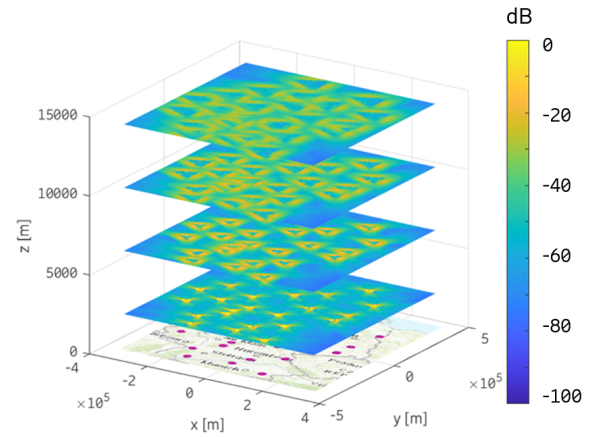


Fig. 10. Normalized combined antenna and path gain coverage plots for (9×1) sub-arrays in the EAN deployment.

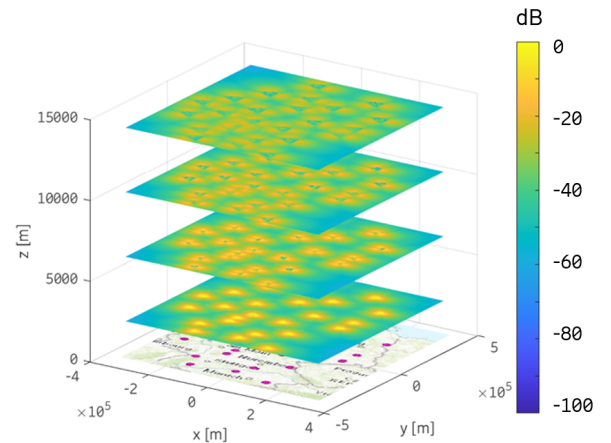


Fig. 11. Normalized combined antenna and path gain coverage plots for (3×1) sub-arrays in the EAN deployment.

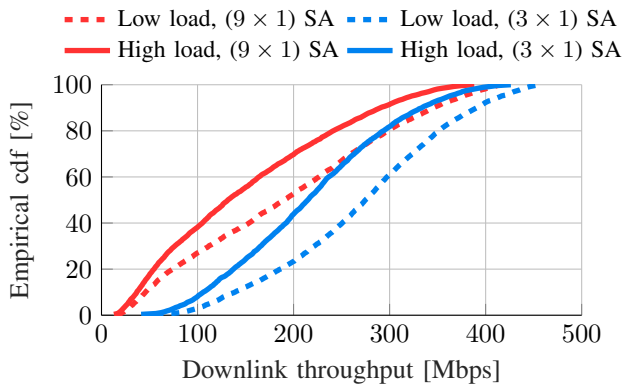


Fig. 12. Downlink throughput cdf in the EAN deployment at 10 km of altitude for different traffic loads and sub-array (SA) configurations.

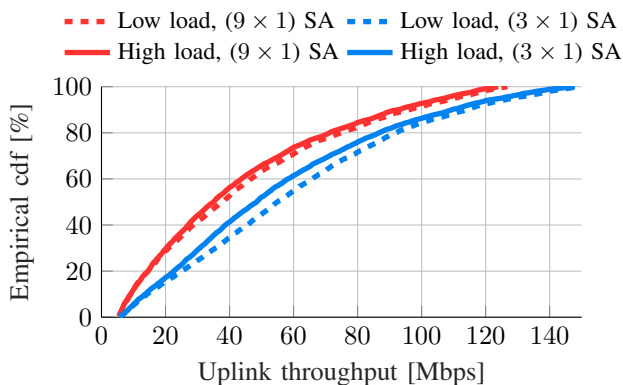


Fig. 13. Uplink throughput cdf in the EAN deployment at 10 km of altitude for different traffic loads and sub-array (SA) configurations.

dimension on throughput is significant in both downlink and uplink direction regardless the cell load, although it is less pronounced in the uplink direction. For example, the median downlink throughput in high load goes from 131 Mbps in the (9×1) configuration to 214 Mbps in the (3×1) arrangement. Overall, it is crucial to have the correct antenna dimensioning for the ATG deployment of interest to obtain the best coverage performance and throughput performance.

IV. CONCLUSION

The paper presents a ground BS antenna design for the cmWave band and examined how the antenna array dimension affects the SINR and throughput in ATG systems. The presented ATG system-level simulations indicate that arrays of sub-arrays with smaller sub-array dimensions lead to superior performance than systems with larger sub-array dimensions. This is because the former setup offers larger beamwidth and therefore improves coverage. The simulation results discussed in this paper reveal that sub-optimal antenna array dimensioning can lead to significant throughput losses.

Future work shall address limitations of the paper and provide more insights into some particular aspects of ATG networks. While this work has considered the 7 GHz frequency for ATG communications, it can be problematic from the perspective of coexistence with existent services, e.g.,

satellite links. In this sense, the antenna design and the precoding schemes can be tailored to reduce interference and enable coexistence and alternative frequency ranges might be considered. While the presented coverage analysis has been based solely on system-level simulation, a more formal and analytical approach might provide additional insights.

ACKNOWLEDGMENTS

This work was partially funded by EU Celtic Next Project, 6G for Connected Sky (6G-SKY) with support of the Federal Ministry for Economic Affairs and Climate Action under the contract number 01MJ22010B, Vinnova, Swedish Innovation Agency, the Austrian Federal Ministry for Climate Action, Environment, Energy, Mobility Innovation and Technology via the Austrian Research Promotion Agency (FFG) and Hungarian National Research, Development and Innovation Office, under the agreement no. 2020-1.2.3-EUREKA-2021-000006. The views expressed herein can in no way be taken to reflect the official opinion of the German ministry.

REFERENCES

- [1] Q. Zhao, N. Saxena *et al.*, “White paper: 6G drivers and vision,” NGMN Alliance, Tech. Rep., 2021.
- [2] L. Ibbetson and J. Erfanian, “White paper: 6G position statement,” NGMN Alliance, Tech. Rep., 2023.
- [3] G. Wikström, P. Persson *et al.*, “White paper: 6G – Connecting a cyber-physical world,” Ericsson, Tech. Rep. GFTL-20:001402, February 2022.
- [4] Ericsson, “What is digital airspace?” Available online at: <https://www.ericsson.com/en/blog/2023/6/what-is-digital-airspace>.
- [5] M. Özger, I. Gódor *et al.*, “6G for Connected Sky: A vision for integrating terrestrial and Non-Terrestrial Networks,” *arXiv preprint arXiv:2305.04271*, 2023.
- [6] A. Baltaci, E. Dinc *et al.*, “A survey of wireless networks for future aerial communications (FACOM),” *IEEE Communications Surveys & Tutorials*, vol. 23, no. 4, pp. 2833–2884, 2021.
- [7] Gogo Networks, “Gogo 5GTM: High-speed, ATG broadband for aviation,” Gogo business aviation, Tech. Rep., 2021.
- [8] Alcatel Lucent, “White paper: Using air-to-ground LTE for in-flight ultrabroadband,” Nokia, Tech. Rep., 2015.
- [9] Deutsche Telekom, “European Aviation Network photos,” Available online at: <https://www.telekom.com/de/medien/mediencenter/fotos/fotos-european-aviation-network>.
- [10] M. Sakamoto and S. Kawato, “Four-dimensional network simulation of direct air to ground LTE networks,” in *Proc. 2016 1st International Workshop on Link and System Level Simulations (IWSLS)*, 2016, pp. 1–6.
- [11] E. Dinc, M. Vondra, and C. Cavdar, “Total cost of ownership optimization for direct air-to-ground communication networks,” *IEEE Transactions on Vehicular Technology*, vol. 70, no. 10, pp. 10 157–10 172, 2021.
- [12] X. Lin, A. Furskär *et al.*, “Sky high 5G: New radio for air-to-ground communications,” *5G and Beyond: Fundamentals and Standards*, pp. 503–515, 2021.
- [13] Ericsson, “Co-existence simulation parameters,” in *3GPP TSG-RAN WG4 Meeting #105, R4-2219636*, 2022.
- [14] —, “Initial simulation results,” in *3GPP TSG-RAN WG4 Meeting #105, R4-2219637*, 2022.
- [15] D. Cavallo, A. Neto, and G. Gerini, “Analysis of common-mode resonances in arrays of connected dipoles and possible solutions,” in *Proc. 2009 European Radar Conference (EuRAD)*, pp. 441–444.
- [16] H. Asplund, J. Karlsson *et al.*, *Advanced antenna systems for 5G network deployments: bridging the gap between theory and practice*. Academic Press, 2020.
- [17] K.-L. Wu, C. Wei *et al.*, “Array-antenna decoupling surface,” *IEEE Transactions on Antennas and Propagation*, vol. 65, no. 12, pp. 6728–6738, 2017.
- [18] H. Wang, D.-G. Fang, and Y. L. Chow, “Grating lobe reduction in a phased array of limited scanning,” *IEEE Transactions on Antennas and Propagation*, vol. 56, no. 6, pp. 1581–1586, 2008.
- [19] A. Colpaert, E. Vinogradov, and S. Pollin, “3D beamforming and handover analysis for UAV networks,” in *Proc. 2020 IEEE Globecom Workshops*, 2020, pp. 1–6.